Published online 21 September 2022 *Nucleic Acids Research, 2022, Vol. 50, No. 18* ***10249–10263***
https://doi.org/10.1093/nar/gkac811

Switching G-quadruplex to parallel duplex by molecular rotor clustering

Qiuda Xu, Mujing Yang, Yun Chang, Shuzhen Peng, Dandan Wang, Xiaoshun Zhou and Yong Shao*

Key Laboratory of the Ministry of Education for Advanced Catalysis Materials, College of Chemistry and Life Sciences, Zhejiang Normal University, Jinhua, 321004, China

Received May 05, 2022; Revised August 31, 2022; Editorial Decision September 01, 2022; Accepted September 10, 2022

ABSTRACT

Switching of G-quadruplex (G4) structures between variant types of folding has been proved to be a versatile tool for regulation of genomic expression and development of nucleic acid-based constructs. Various specific ligands have been developed to target G4s in K^+ solution with therapeutic prospects. Although G4 structures have been reported to be converted by sequence modification or a unimolecular ligand binding event in K^+-deficient conditions, switching G4s towards non-G4 folding continues to be a great challenge due to the stability of G4 in physiological K^+ conditions. Herein, we first observed the G4 switching towards parallel-stranded duplex (psDNA) by multimolecular ligand binding (namely ligand clustering) to overcome the switching barrier in K^+. Purine-rich sequences (e.g. those from the KRAS promoter region) can be converted from G4 structures to dimeric psDNAs using molecular rotors (e.g. thioflavin T and thiazole orange) as initiators. The formed psDNAs provided multiple binding sites for molecular rotor clustering to favor subsequent structures with stability higher than the corresponding G4 folding. Our finding provides a clue to designing ligands with the competency of molecular rotor clustering to implement an efficient G4 switching.

GRAPHICAL ABSTRACT

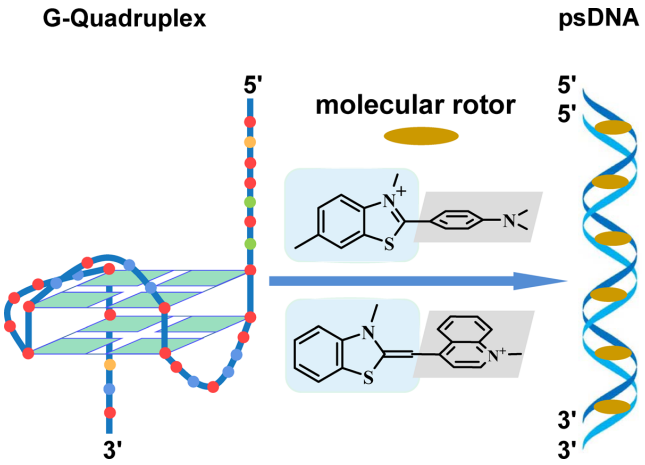

INTRODUCTION

Since the discovery of the canonical double-stranded antiparallel DNA structure, some non-canonical DNA structures including parallel-stranded DNA (1,2), Z-DNA (3,4), i-motif (5,6), triplex (7,8) and G-quadruplex (G4) (9–17) have been found to also take part in the cellular process (5,6,9,18,19). Besides their unique biological activities, these non-canonical structures have also attracted considerable attention in fabrication of multifunctional devices (20,21), switches (22,23) and biomaterials (24). Due to the close relationship of diseases with G4 structures (10–16), considerable efforts have been made to switch G4 conformations using variant initiators. The first initiators are the intrinsic sequence modulators (25–27). For instance, the introduction of an apurinic site in the G tract (25) or in the loop (26) is a common strategy to enable transformation from one type of G4 folding to another (GF1→GF2) for human telomeric G4 (htG4). Replacement of guanine with an oxidized analog (such as 8-oxo-7,8-dihydroguanine) in the G tract of the promoter region of the human vascular endothelial growth factor (VEGF) alters the original

*To whom correspondence should be addressed. Email: yshao@zjnu.cn

parallel folding to a mixed G4 topology (27). Additionally, replacement of natural β-dGs with α-dGs in the telomere sequences of *Oxytricha nova* can convert the antiparallel G4s to parallel ones (GF1→GF2) (28). The second initiators are external environment factors including pH (29,30), solvent (31–33), molecular crowding (34–36) and light irradiation (37,38). For example, the htG4 sequence with one guanine truncated at the 3′ end allows a structure conversion from one type of the basket antiparallel folding to another (GF1→GF2) upon changing the solution pH from neutrality to acidity. This conversion is caused by protonation of the adenine in the third loop to favor a capping triad beyond the G-quartet (30). However, in deep eutectic solvent, htG4 is converted to a parallel folding different from the hybrid structure formed in aqueous K^+ solution (32,33). This GF1→GF2 transformation towards parallel foldings also occurs for htG4 and the telomere G4 of *Oxytricha nova* using polyethylene glycol (PEG) as the molecular crowding reagent (34–36). In addition, Tan *et al.* (37) used PEG to covalently link the thrombin-binding aptamer (TBA) and the azobenzene-modified complementary sequence. The *cis*-form of the azobenzene moieties did not favor duplex formation and the G4 structure remained intact. However, visible light irradiation converted the *cis*-form to the *trans*-form in favor of switching the G4 structure to a hairpin duplex structure (H-DNA) with a restored thrombin activity, and UV light irradiation reversed this conversion (i.e. GF↔H-DNA). Furthermore, a fluorenylvinyl-modified guanine converter was able to reversibly switch TBA between the G4 structure and the unfolding state (GF↔U) by photoisomerizing the converter between the *cis*- and *trans*-forms in K^+ solution (38). Although the sequence modulators and environmental factors are very helpful to elucidate the determinants in governing the G4 conformations, alternative initiators are actually needed to achieve the G4 structure regulation when these two former initiators cannot be used in the case of, for example, label-free and environmentally determined requirements. In this aspect, the third initiators of specific ligands are more practical in switching the G4 structures for variant applications such as helicase mimics (39,40). In this respect, Monchaud *et al.* (41) and Balasubramanian *et al.* (42) made efforts to screen disrupters over htG4 and the proto-oncogene c-*kit* G4, and found that the phenylpyrrolocytosine and triarylpyridine derivatives were efficient to break these G4 structures (GF→U). In K^+-deficient solution, reversibly switching htG4 between folding and unfolding states (GF↔U) was realized using azobenzene derivatives as the G4-binding ligands and employing photoisomerization (43) and supramolecular encapsulation (44) as the dynamic initiators. Alternatively, in Na^+ solution, a stiff-stilbene was used as a fuel ligand to reversibly switch htG4 (GF↔U) by fuel photofragmentation (45). Recently, we found that a polarity inversion in the phosphate backbone can unfold TBA, and a natural isoquinoline alkaloid can restructure it into an antiparallel G4 assembly in K^+ (U→GF) (46). Despite these efforts, developing ligand initiators with a versatile G4 switching competency in physiological K^+ conditions is a continuously great challenge in comparison with the sequence modulators and environmental factors.

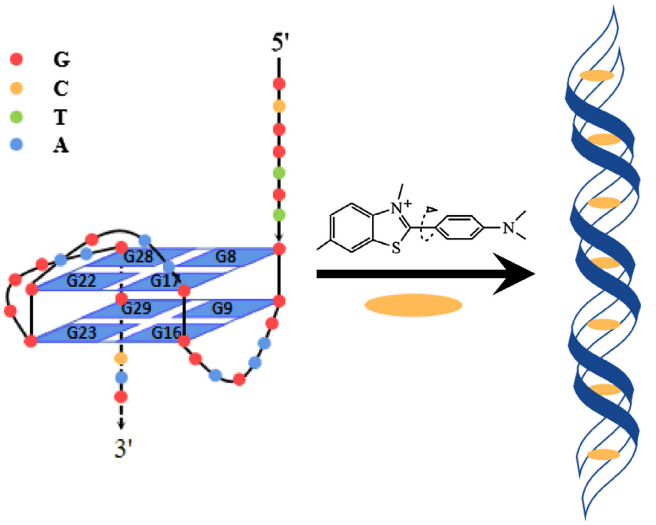

Scheme 1. Schematic diagram of G4 switching to psDNA by ligand clustering.

In this work, to overcome the usual inability of a single binding ligand to switch G4, we investigated the switching of G4 towards a parallel-stranded duplex structure (GF→psDNA) by ligand clustering, for the first time. We expect that the multimolecular binding sites in the converted psDNA will cluster the ligand population to drastically stabilize the psDNA structure and provide the chance to switch G4 structures in K^+ without any modification of G4 sequences. The upstream nuclease-hypersensitive elements (NHE) of the transcription start site (TSS) in the human KRAS proto-oncogene can form G4 structures within the far, mid and near regions separated by tens of nucleotides (47–51). The sequence of 32R (Table 1) in the near region mainly folds into a parallel G4 structure (47,51–58), while the sequence with a 3 nt frameshift towards the 3′ direction (namely, 32R-3n, Table 1) adopts dose-dependent structures other than parallel folding: the unimolecular hybrid G4 at low concentration (59,60), and the dimeric antiparallel G4 at high concentration (61). Switching the G4 structures in this region by ligands is a promising way to regulate the gene expression (47,50,52,56,62,63). Herein, molecular rotor (MR) probes were used as the clustering ligands to implement the GF→psDNA switching (Scheme 9). The MR probes [thioflavin T (ThT) and thiazole orange (TO)] can interact with variant DNA structures (64) including an abasic site (65), guanine (66,67) or AT (68) island, loop (69), i-motif (70) and G4 (71–75). More interestingly, following the leading work of Li's group (2), several researchers have confirmed the ThT-induced psDNA formation for single-stranded GA-rich sequences (76,77). These DNA interactions subsequently turn on the MR fluorescence, dependent on the binding modes, DNA structures and sequences (78). However, the G4 switching by the MR clustering rationale has not been elucidated.

Table 1. DNA sequences used in this work

Entry	Sequence	Remark
32R-3n	5′-GCGGTGTGGGAAGAGGGAAGAGGGGGAGGCAG-3′	
32R-3n-2AP	5′-GCGGTGTGGGAAGAGGGAAGAGGGGG**N**GGCAG-3′	N = 2-aminopurine, 2-AP
32R-3n-3P	5′-GCGGTGTGGGAAGAGGGAAGAGGGGGAGGCAG-3′-P	pyrene (P) at the 3′ end
5–7T	5′-TTTTTTTGGGAAGAGGGAAGAGGGGGAGGCAG-3′	
5–7D	5′-GGGAAGAGGGAAGAGGGGGAGGCAG-3′	
3–8T	5′-GCGGTGTGGGAAGAGGGAAGAGGGTTTTTTTT-3′	
3–8D	5′-GCGGTGTGGGAAGAGGGAAGAGGG-3′	
32R-3n-T11	5′-GCGGTGTGGGTTTTTTTTTTGGGGGAGGCAG-3′	
32R	5′-AGGGCGGTGTGGGAAGAGGGAAGAGGGGGAGG-3′	
22R	5′-AGGGCGGTGTGGGAAGAGGGAA-3′	
22RT	5′-AGGGCGGTGTGGGAATAGGGAA-3′	
X12-1245	5′-TGGGGAGGGTG**X**GGAGGGTGGGGAAGG-3′	X = abasic site
X12-1245-3P	5′-TGGGGAGGGTG**X**GGAGGGTGGGGAAGG-3′-P	pyrene (P) at 3′ end
X12-A3-2345	5′-TGAGGAGGGTG**X**GGAGGGTGGGGAAGG-3′	
X12-A3-2345-3P	5′-TGAGGAGGGTG**X**GGAGGGTGGGGAAGG-3′-P	
dsDNA	5′-(TTAGGG)$_5$TT-3′ 3′-(AATCCC)$_5$AA-5′	

MATERIALS AND METHODS

DNAs and chemicals

DNAs used in this work are listed in Table 1. DNAs (TaKaRa Biotechnology Company, Ltd, Dalian, China) were first dissolved in pure water, and the absorbance at 260 nm was then recorded to obtain the DNA concentration (in the strand) using the extinction coefficient obtained from the nearest-neighbor method. To prepare the DNA solution, the strand was annealed in a thermocycler (first at 92°C, then slowly cooled to room temperature) in 0.02 M Tris–HCl buffer (pH 7.0) containing 0.1 M KCl or LiCl and then stored at 4°C overnight. Thioflavin T (ThT) was obtained from AAT Bioquest, Inc. (Sunnyvale, CA, USA). Thiazole Orange (TO) and 2-(4′-methylaminophenyl)-benzothiazole (BTA-1) were purchased from Sigma Chemical Company (St. Louis, MO, USA). Milli-Q water (18.2 MΩ; Millipore Company, Billerica, MA, USA) was used in all experiments. All other chemicals were analytical-reagent grade and used without further purification.

Fluorescence measurements

Fluorescence spectra were acquired with an FLSP920 spectrofluorometer (Edinburgh Instruments Ltd, Livingston, UK) and the chamber temperature was controlled by a circulator (Julabo Labortechnik GmbH, Seelbach, Germany) at 20 ± 1°C. Fluorescence was measured in a quartz cell with a path length of 1 cm. Ligand at the specified concentration was mixed with the DNA solution; the resulting solution was incubated for 30 min at room temperature and was then equilibrated for 5 min in the chamber before fluorescence determination. The Job's plot analysis was used to fluorescently evaluate the binding stoichiometry of ligand with DNA. The total concentration of ligand and DNA was kept at 2 μM and the concentration ratio was systematically changed. The SFA-20 stopped-flow accessory (TgK Scientific Ltd, UK) was used to fluorescently check the switching kinetics (excitation/emission: 440/490 nm).

DNA melting measurements

The melting temperature (T_m) of DNAs in the presence and absence of ligand was determined using a UV2550 spectrophotometer (Shimadzu Corp., Kyoto, Japan) that was equipped with a TMSPC-8 T_m analysis system. A micro quartz multi-cell with eight cuvettes was used and thus all of the solution temperatures were simultaneously controlled in these cuvettes with a small deviation. The absorbance at 295 nm as a function of solution temperature (79) was used to follow the G4 structure and that at 260 nm was used to monitor the psDNA dimer formation. The data were collected at 0.5°C increments between 5 and 90°C, and an equilibration time of 30 s was applied after each temperature increase. The T_m values were obtained by differentiating the fitted melting curves. To eliminate the effect of the ligand absorbance on the melting jump amplitude, the melting data were normalized to zero at high and low temperatures for the melted G4 and dimer, respectively. The van't Hoff analysis (80) was used to predict the thermodynamic behaviors of 32R-3n melting in K^+ and Li^+ with an excess of ligand.

Circular dichroism spectra measurements

Circular dichroism (CD) spectra were recorded on a MOS-500 CD spectrometer (Bio-Logic Science Instruments, France) using a quartz cuvette with a path length of 2 mm. The scanning speed was 200 nm/min, and the response time was 0.5 s. The presented spectra were the average of three scans. The DNA solution was mixed with ligand at the specified concentration in 0.02 M Tris–HCl buffer (pH 7.0) containing 0.1 M KCl or LiCl, and the resulting solution was incubated for 30 min at room temperature before the CD measurement.

Isothermal titration calorimetry measurements

Isothermal titration calorimetry (ITC) experiments were performed at 20°C using an ITC200 microcalorimeter (MicroCal, LLC, Northampton, MA, USA). DNA and ligand solutions were prepared using an identical 0.02 M Tris–HCl buffer (pH 7.0) containing 0.1 M KCl or LiCl. DNA

(10 μM) in the sample cell was titrated dropwise using a 2 μl ligand injection at the specific concentration (except for the first injection of 0.4 μl for calibration). Each injection was completed within 20 s and an injection interval of 150 s was applied. The titration of ligand in the syringe into the identical buffer solution in the sample cell without DNA was used as a control to obtain the heat of dilution. The area of each injection peak was automatically integrated by Origin (version 9.0) software. A binding isothermal curve was obtained by plotting the total heat per injection (kcal/mol of injectant) as a function of the molar ratio between ligand and DNA.

Electrophoretic mobility shift assay

Non-denaturing 20% polyacrylamide gel electrophoresis (PAGE) was carried out in 1× TBE buffer (pH 8.0) containing 0.1 M KCl or LiCl. A 10 μl aliquot of the annealed DNA solution (8 μM) in the absence and presence of ligand was loaded into the channel. Gel electrophoresis was run at 4°C in the same buffer under a voltage of 60 V for 6 h or of 110 V for 2 h. Then the gel was stained in 0.01% Stains-All solution and photographed with a camera. Black and white pictures were finally presented. For the hydroxylation experiments of ThT (81), prior to PAGE, ThT in the absence and presence of DNA was kept at 50°C for 6 h in 0.02 M Tris–HCl buffer (pH 9.0). A control experiment was carried out at 25°C at which the hydroxylation occurred much less often. After cooling to room temperature, the solution was mixed with DNA if necessary in 1× TBE buffer containing 0.1 M KCl.

RESULTS

ThT-induced dimer formation of the KRAS G4 sequences

CD spectra were first used to investigate the binding behavior of ThT with the KRAS G4s. 32R-3n in K^+ gave two positive bands at 294 and 262 nm, and a negative band at 242 nm (Figure 1A), in accordance with the CD responses of 32R-3n adopting a hybrid G4 folding (Figure 1C), that was suggested by the L.E. Xodo group, with three loops (the first 6 nt loop of 5′-GAAGAG-3′, the second 4 nt loop of 5′-AAGG-3′ and the third 4 nt loop of 5′-GGGA-3′), a 7 nt 5′ overhang of 5′-GCGGTGT-3′ and a 3 nt 3′ overhang of 5′-CAG-3′ (60), respectively. However, the corresponding bands at only 262 and 242 nm were also observed for 32R-3n incubated in Li^+. This could be caused mainly by the random coil of 32R-3n with purine-rich sequences (2,82). Another hybrid G4 structure with the 8 nt 3′ overhang of 5′-GGAGGCAG-3′ (the underlined base is A27) has also been proposed for the pyrene derivative-inserted 32R-3n (59). To exclude this folding possibility, we replaced A27 in 32R-3n with an analog of 2-aminopurine (2-AP) to obtain 32R-3n-2AP and found that the fluorescence of 32R-3n-2AP at 365 nm in K^+ was ∼17-fold higher than that in Li^+ (Figure 1D), suggesting that 2-AP exists in different environments in these two cases. This implies that most of the 32R-3n in K^+ solution folds into a G4 structure and the folding with involvement of the 8 nt 3′ overhang has less chance to take place. The 32R-3n folding in K^+ proposed in Figure 1C will expose the 2-AP label to a greater degree than the unstructured folding in Li^+, in accordance with the fluorescence results as shown in Figure 1D. To eliminate effects of the loop and overhang bases on the CD spectra, we subtracted the CD spectrum of 32R-3n obtained in Li^+ from that obtained in K^+, and the resultant CD difference spectrum featured two positive bands at 294 and 245 nm, and a small valley at 260 nm (Supplementary Figure S1), characteristic of a hybrid G4 structure (83,84). Interestingly, with addition of ThT, the positive band of 32R-3n at 262 nm in K^+ significantly increased, while the positive band at 294 nm disappeared. This disappearance suggests that the antiparallel G4 dimer as suggested by the Xodo group for 32R-3n at high DNA concentration is not possible in our experimental conditions (61). Note that the induced CD (ICD) band at 445 nm appeared with ThT binding. More importantly, 32R-3n in Li^+ with the presence of ThT gave the same ICD profile as in K^+ (Figure 1A). These results suggest that the ThT binding dominates a new structure other than G4, as suggested by independence of the cation identity (K^+ and Li^+) on the CD responses of 32R-3n. The time-dependent fluorescence increase of ThT upon binding with 32R-3n demonstrated formation of the new DNA structure within tens of seconds in either K^+ or Li^+ (Supplementary Figure S2). This newly formed structure should be a ThT-stabilized parallel-stranded duplex (psDNA) as proposed by the previous works for purine-rich sequences (2,76,77,85–87). The only negative ICD band of ThT indicates an intercalation binding with the ThT transition moment orienting perpendicular to the duplex pseudo-dyad (71,88). In contrast, we then investigated the CD responses of 32R (Table 1) with the 3 nt frameshift relative to 32R-3n, and a positive band at 262 nm and a negative band at 242 nm in K^+ were observed (Figure 1B), indicative of a dominant parallel G4 structure as shown in Figure 1C (58). However, ThT addition did not change the CD contour of 32R, suggesting preservation of the G4 structure in K^+. When these experiments were carried out in Li^+, with the ThT addition, a significant increase in the CD band at 262 nm was also observed, with the appearance of an obvious and negative ICD band at 445 nm (Figure 1B), as occurred for 32R-3n in either K^+ or Li^+. Therefore, ThT only in Li^+ (but not in K^+) should induce 32R to form the psDNA structure.

The PAGE experiments (Figure 1E) showed that both 32R-3n and 32R (8 μM) in K^+ led to single migration bands with the same mobility, indicating that 32R-3n as well as 32R formed a single dominant G4 structure in K^+. However, the presence of ThT (20 μM) retarded the 32R-3n migration in K^+, with the migration velocity similar to that of the 64 nt double-stranded DNA (dsDNA) marker [5′-$(TTAGGG)_5$TT-3′/3′-$(AATCCC)_5$AA-5′], as opposed to 32R in K^+ exhibiting unchanged migration upon ThT binding. These results mean that the formed G4 structure of 32R-3n in K^+ can be disrupted by ThT to form a psDNA dimer, but 32R is inefficient with this switching. Gradually increasing the ThT concentration blurred the G4 band of 32R-3n and concurrently developed the dimer band, and 5 μM ThT was enough to visualize the dimer band (Figure 1F), while this did not occur for 32R (Supplementary Figure S3). This demonstrates the role of the 3 nt frameshift in switching the G4 structure by ThT. When these PAGE

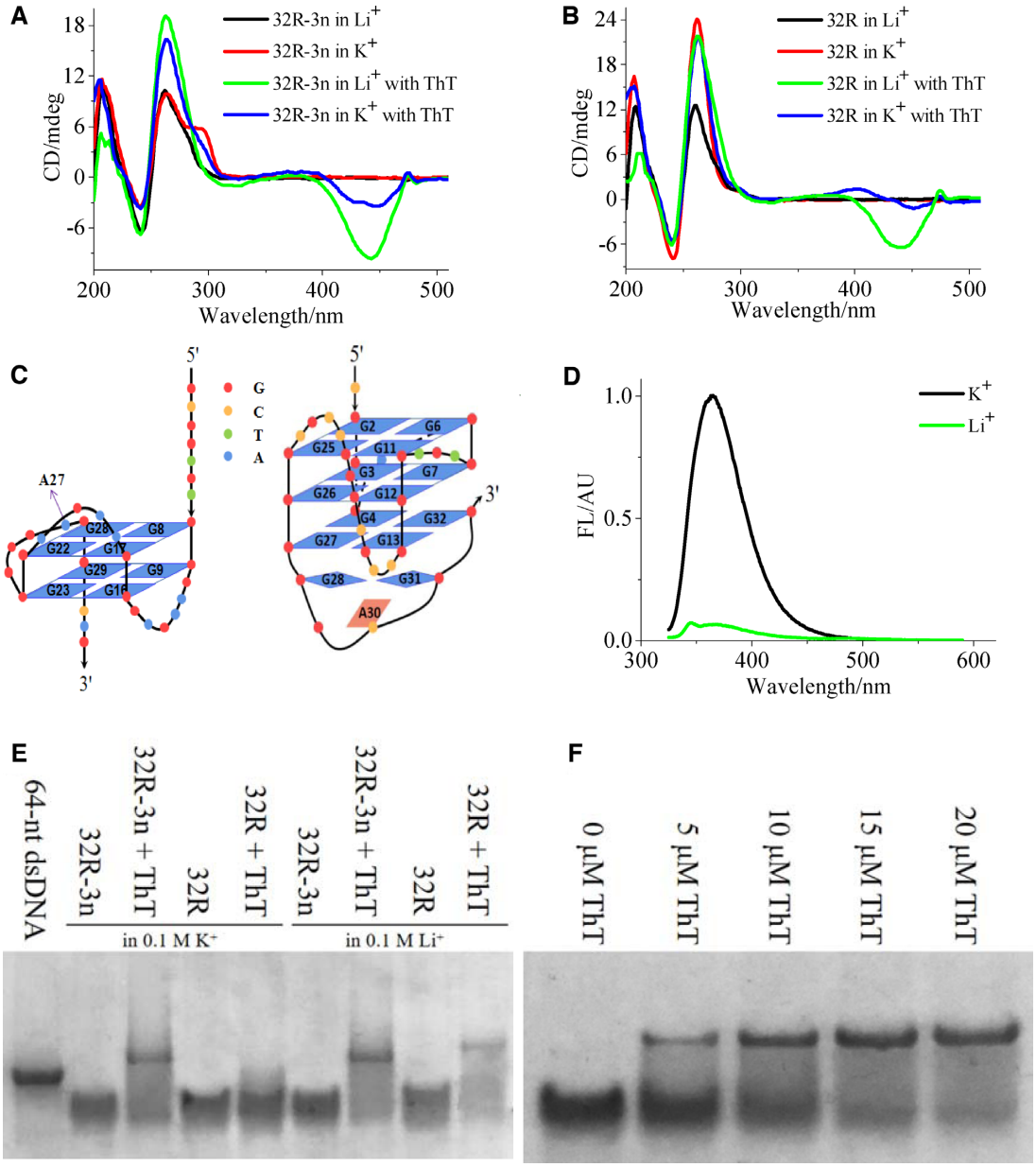

Figure 1. CD spectra of (**A**) 32R-3n and (**B**) 32R (8 μM) with or without 160 μM ThT in 0.02 M Tris–HCl (pH 7.0) containing 0.1 M K^+ or Li^+. (**C**) Typical structures of (left) 32R-3n and (right) 32R in K^+ according to previous studies. The substituent site in 32R-3n-2AP by 2-aminopurine (2-AP) is A27. (**D**) Emission spectra of 32R-3n-2AP in 0.02 M Tris–HCl (pH 7.0) containing 0.1 M K^+ and Li^+. Excitation: 305 nm. (**E**) PAGE diagram of 32R-3n and 32R (8 μM) with or without 20 μM ThT in 0.1 M K^+ or Li^+. (**F**) PAGE diagram of 32R-3n (8 μM) with increasing ThT concentration in 0.1 M K^+.

experiments were carried out in Li^+, with ThT addition, both 32R-3n and 32R migrated as sluggishly as 32R-3n in K^+ (Figure 1E). Therefore, ThT in Li^+ can lead to psDNA dimer formation for both 32R-3n and 32R, as suggested by the previous reports for the purine-rich sequences devoid of G4-forming competency (2,76,77).

Relative stabilities of G4 and dimer regulate the structure switching

As demonstrated by previous reports (47–61), the G4 structure of 32R-3n in K^+ was less stable than that of 32R. Herein, we determined their T_m in 0.1 M K^+ to be ~50.9°C and 62.7°C by following the absorbance at 295 nm as a function of the solution temperature (Figure 2A). To monitor the duplex formation upon G4 switching, the melting behaviors were then measured at 260 nm with ThT addition. Indeed, the melting jump amplitude of 32R-3n in K^+ and Li^+ gradually increased upon increasing the ThT concentration (Figure 2B, C). At 40 μM ThT, the T_m values of 32R-3n increased to ~58.0°C in both K^+ and Li^+, with the ΔT_m values being ~7.1 and 19.8°C, respectively (Figure 2D). The van't Hoff analysis (Supplementary Figure S4) also predicted the same thermodynamic melting behaviors of 32R-3n in K^+ and Li^+ at this ThT concentration. These results indicate that ThT can not only stabilize psDNA, but

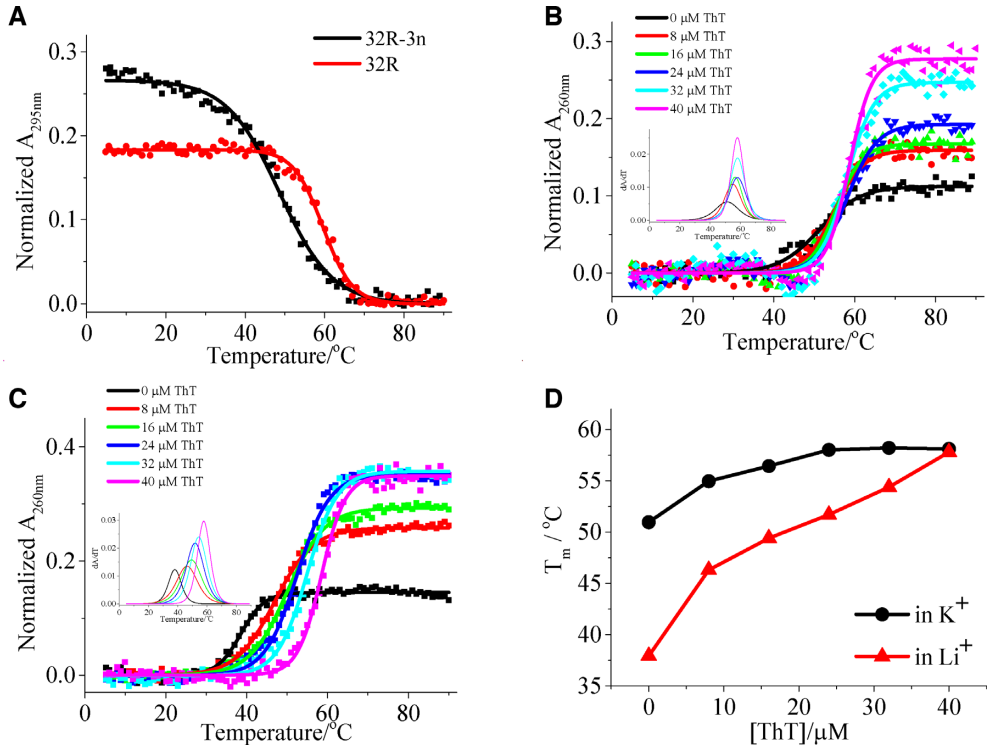

Figure 2. (**A**) Melting curves of 32R and 32R-3n (4 μM) in 0.02 M Tris–HCl (pH 7.0) containing 0.1 M K^+ monitored at 295 nm. (**B** and **C**) Melting curves of 32R-3n (4 μM) monitored at 260 nm in 0.02 M Tris–HCl (pH 7.0) containing 0.1 M (**B**) K^+ and (**C**) Li^+ with addition of ThT. Inset: first-order derivation diagrams of the melting curves. (**D**) The fitted T_m values as a function of the ThT concentration.

can also transform 32R-3n from the hybrid G4 structure to the more stable psDNA in K^+ solution. However, the addition of ThT to the K^+ solution of 32R increased the T_m value from 62.7 to 66.9°C (40 μM ThT),as obtained by following the temperature-dependent absorbance at 295 nm, while the T_m value of 32R in Li^+ monitored at 260 nm increased from 34.0 to 51.3°C (40 μM ThT) (Supplementary Figure S5). Therefore, the ThT-stabilized psDNA of 32R is much less stable than its G4 structure. Thus, unlike the ThT-induced 32R-3n switching, 32R in K^+ cannot be converted into the psDNA dimer, as observed in the CD and PAGE experiments shown in Figure 1B and E.

The psDNA dimer formation evidenced by pyrene excimer emission

We modified 32R-3n with a pyrene molecule at the 3′ end (32R-3n-3P, Table 1) to follow the psDNA dimer formation due to separation of the monomer and excimer emission bands (89). 32R-3n-3P in K^+ had a monomer emission band between 350 and 450 nm (with excitation at 348 nm) and no excimer band was observed (Figure 3A), while in Li^+ the monomer emission band slightly decreased (to be ∼75% of that in K^+) and a small excimer band appeared at 480 nm (Figure 3B). This small excimer band could be caused by a partial formation of the dimer structure in Li^+ that was favored by the hydrophobicity of the labeled pyrene, or somewhat by the effect of the ion identity. Upon ThT addition, the monomer emission band decreased with a concomitant increase in the excimer emission band in either K^+ or Li^+, indicative of the ThT-induced dimer formation. Since the emission band of ThT (490 nm) was overlapped by the pyrene excimer band (480 nm), we subtracted the ThT emission obtained using 32R-3n (Supplementary Figure S6) from that of 32R-3n-3P under the identical experimental condition to correct the excimer emission, although the ThT emission was relatively low at the excitation wavelength for pyrene (348 nm). The emission band area was used to quantify the monomer consumption and the dimer formation. The G4 population was quantified with respect to the monomer emission band of 32R-3n-3P alone in K^+, while the dimer population was quantified with respect to the excimer emission band of 32R-3n-3P in the presence of an excess of ThT in Li^+. Figure 3C and D demonstrate the relative conversion of 32R-3n in K^+ and Li^+ between the G4 structure and the dimer. With the presence of enough ThT, the majority of the G4 structure formed in K^+ can be converted to the psDNA dimer structure (∼90% of that formed with an excess of ThT in Li^+). Therefore, by combining the results of the CD experiments with the disappearance of the 294 nm band caused by ThT (Figure 1A), the possible inter-G4 dimer linking together the intact G4 structure through the overhangs by ThT as depicted in Figure 3E can be ruled out.

The binding site of ThT in the psDNA dimer

32R-3n-2AP with A27 in 32R-3n replaced by 2AP was used to evaluate the ThT-binding sites in the psDNA dimer. It has been reported that the ThT binding dominantly occurs at the 5′-GA-3′ step of the purine-rich psDNA structures (2,76,77). Therefore, the G26-2AP step should also be the

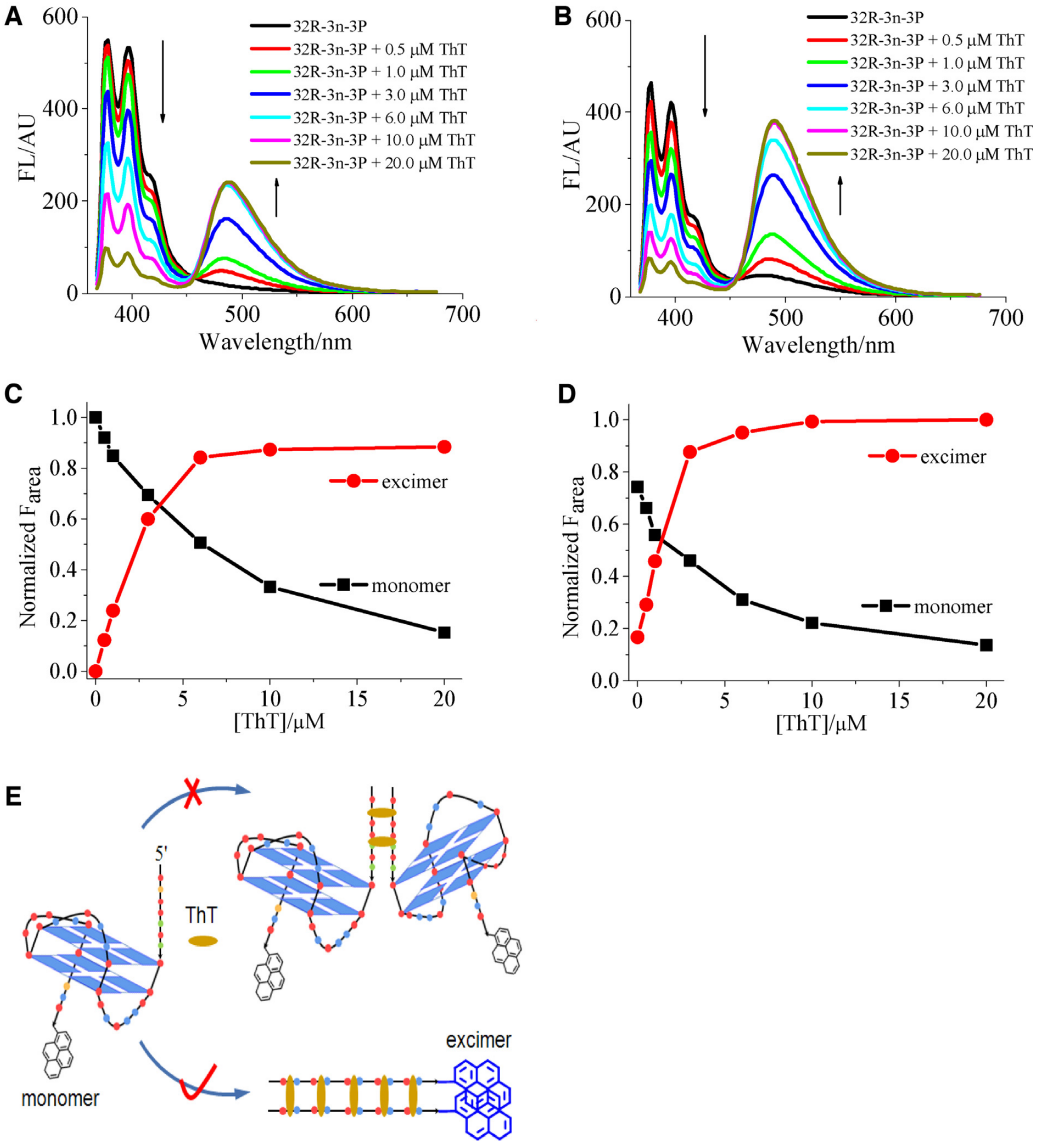

Figure 3. (**A** and **B**) Emission spectra of 32R-3n-3P (1 μM) with addition of ThT in 0.02 M Tris–HCl (pH 7.0) containing 0.1 M (A) K^+ and (B) Li^+. Excitation: 348 nm. (**C** and **D**) Normalized emission band areas of the monomer and excimer 32R-3n-3P (1 μM) with addition of ThT in (C) K^+ and (D) Li^+ with respect to the area of the monomer band of 32R-3n-3P alone in K^+ and that of the excimer band saturated by ThT in Li^+, respectively. The ThT emission in the presence of 32R-3n (1 μM) with excitation at 348 nm was correspondingly subtracted from that of 32R-3n-3P to show only the excimer emission. (**E**) The ThT preference for the psDNA formation over the inter-G4 dimer.

ThT-binding site and thus favor the occurrence of fluorescence resonance energy transfer (FRET) between the excited 2AP and the inserted ThT since the emission band of 2AP partially overlaps the excitation band of ThT (Supplementary Figure S7), although the 2AP fluorescence in the psDNA environment should be somewhat quenched (as indicated in Figure 1D). To correct the ThT emission at the excitation of 305 nm for 2AP, we subtracted the spectra of 32R-3n from those of 32R-3n-2AP at each of the ThT concentrations used, and the resultant differential emission spectra are shown in Figure 4A. Indeed, the FRET occurrence was observed with an increase of the ThT emission band at the expense of the 2AP band (Figure 4B), suggesting that the 5′-GA-3′ step is indeed the ThT-binding site.

We also observed that the fluorescence behaviors of ThT upon binding to 32R-3n at 490 nm in K^+ and Li^+ were strongly dependent on the [ThT]/[32R-3n] ratio, as depicted in Figure 4C. At 8 μM 32R-3n, the fluorescence increased to a vertex in either K^+ or Li^+, with the [ThT]/[32R-3n] ratio increasing up to ∼3–3.5 and, beyond this ratio, the fluorescence experienced a decrease, most probably due to the quenching effect of the post-bound ThT with the preformed psDNA by other binding modes at high ThT concentration on the pre-inserted ThT responsible for the psDNA formation (78). This vertex ratio means that 6–7 ThT molecules may be needed to switch G4 to the psDNA structure, suggestive of the role of molecule clustering in G4 switching. However, this vertex was not observed with 32R-3n at 1 μM. These results suggest that a high 32R-3n con-

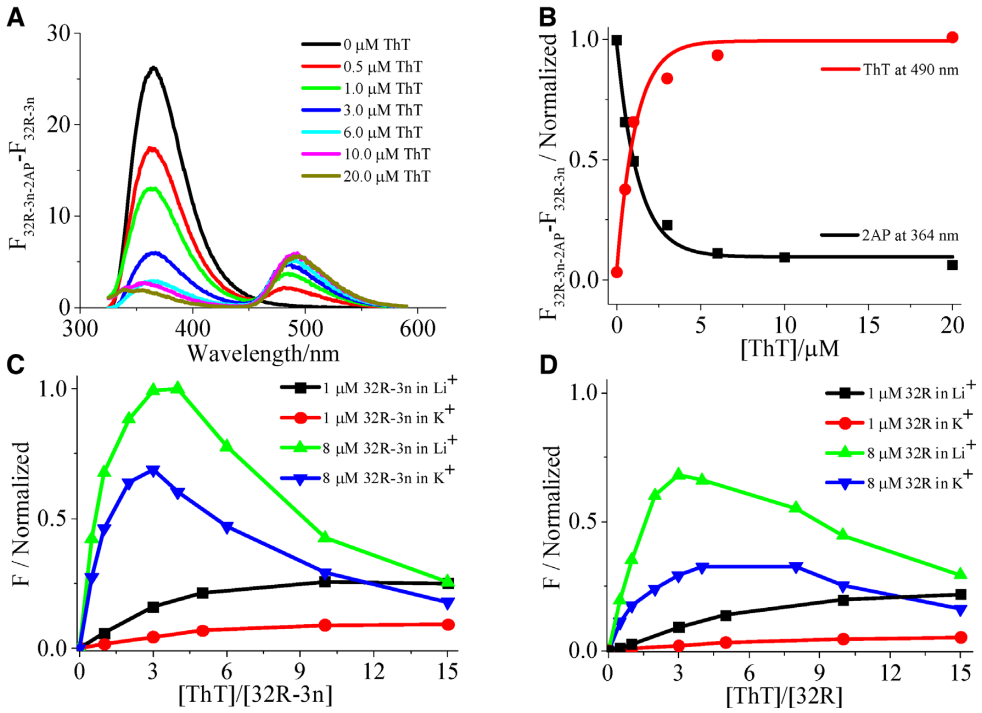

Figure 4. (**A**) Fluorescence differential spectra of 32R-3n-2AP against 32R-3n (1 μM) with ThT addition in 0.1 M K^+. Excitation: 305 nm. (**B**) The normalized fluorescence intensities of 2AP at 365 nm and ThT at 490 nm as a function of the ThT concentration. (**C** and **D**) Effect of the DNA concentration (1 and 8 μM) on the [ThT]/[DNA] ratio-dependent fluorescence response in 0.1 M K^+ and Li^+. The data for (D) 32R were normalized with respect to (C) 32R-3n at 8 μM in Li^+.

centration favors DNA molecules approaching each other to form the dimer under ThT initiation. On the other hand, when 32R was tested using the same procedure, the same and obvious vertex ratio was observed only in Li^+ with the high 32R concentration (Figure 4D), indicative of the favored psDNA formation in Li^+, which is consistent with the PAGE results shown in Figure 1.

Molecular rotor clustering in regulating the dimer formation

The 32R-3n binding in K^+ red-shifted the absorption spectra of ThT from 410 nm to 440 nm (Figure 5A), compared with the smaller shift for 32R binding (only to 425 nm with a ThT concentration up to 4 μM, Figure 5B). The absorbance at 440 nm as a function of the DNA concentration was also shown in Figure 5C to demonstrate the binding preference. In addition, the presence of 32R-3n (1 μM) increased the fluorescence of ThT (20 μM) by 430-fold, twice that of the 32R response (Figure 5D). In addition, the ThT insertion into 32R-3n was evidenced by the slightly altered fluorescence with extra addition of Li^+ into the K^+ solution, as compared with the obvious decrease of the 32R-induced ThT fluorescence with increasing Li^+ concentration (inset of Figure 5D). Furthermore, it has been reported that ThT can be hydroxylated in basic solution upon heating, and its DNA binding capacity will be weakened (71,81). We herein found that the pre-hydroxylated ThT before the 32R-3n binding did not cause the GF→psDNA switch, while the pre-incubation of 32R-3n protected ThT from hydroxylation and the dimer formation was not affected (Supplementary Figure S8), strongly suggesting insertion of ThT into the psDNA dimer. These results indicate that the DNA binding restructures the relative orientation of the benzothiazole (BZT) and aminobenzene (AB) rings of ThT and limits their mutual rotation (Figure 6A) to favor the radiative transition via suppression of the non-radiative twisted internal charge-transfer (TICT) process (71,90–92). We expect that just the molecular rotor rationale is responsible for the DNA switching observed herein. The flexible rotor can be more adaptive to the psDNA base-pair stacking, such as the ThT-binding sites of the 5′-GA-3′/5′-GA-3′ steps.

To confirm this molecular rotor rationale, a ThT analog of BTA-1 (having the same ring skeleton, Figure 6A) was used as a control. In contrast to ThT, BTA-1 is coplanar between the two rings, due to loss of the methyl group in the BZT ring, and thus is not a molecular rotor (71,93). As expected for a non-rotor molecule, BTA-1 was fluorescent alone in aqueous solution and the presence of 32R-3n did not alter its fluorescence response (Supplementary Figure S9A). As demonstrated also by the PAGE experiments (Figure 6B), there was indeed no dimer formation for 32R-3n when incubated with BTA-1 in either K^+ or Li^+, suggesting the molecular rotor rationale in regulating the psDNA dimer formation.

A ThT-analogous cyanine dye of TO (Figure 6A) was then employed as another molecular rotor ligand (94–96). TO consists of the BZT ring and a quinoline (QU) ring, and the rotation of the QU ring with respect to the methine chain causes a non-radiative deactivation of its excited state (96). As a staining dye, TO can bind with variant DNA structures including G4 (74,75). As for the ThT rotor, the 32R-3n binding in K^+ caused an increase in the TO flu-

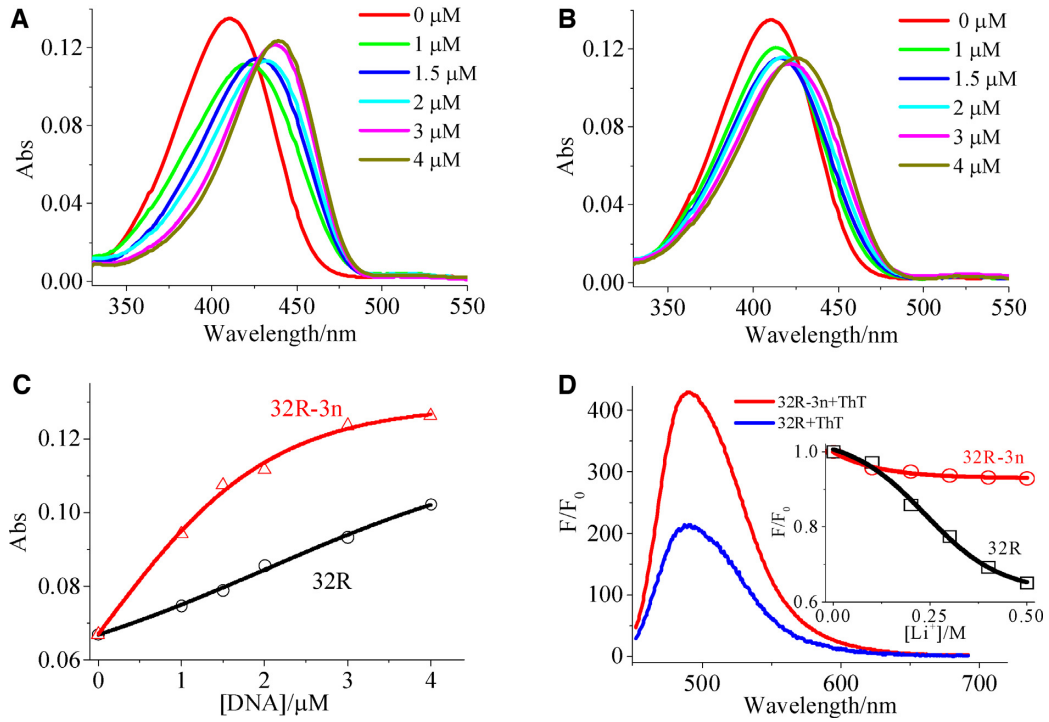

Figure 5. (**A** and **B**) Absorption spectra of ThT (5 μM) in 0.1 M K^+ with increasing concentration of (A) 32R-3n and (**B**) 32R. (**C**) The absorbance of ThT at 440 nm as a function of the DNA concentration. (**D**) Fluorescence emission spectra of ThT (20 μM) in 0.1 M K^+ with the presence of DNA (1 μM). Excitation: 440 nm. Inset: effect of extra Li^+ concentration.

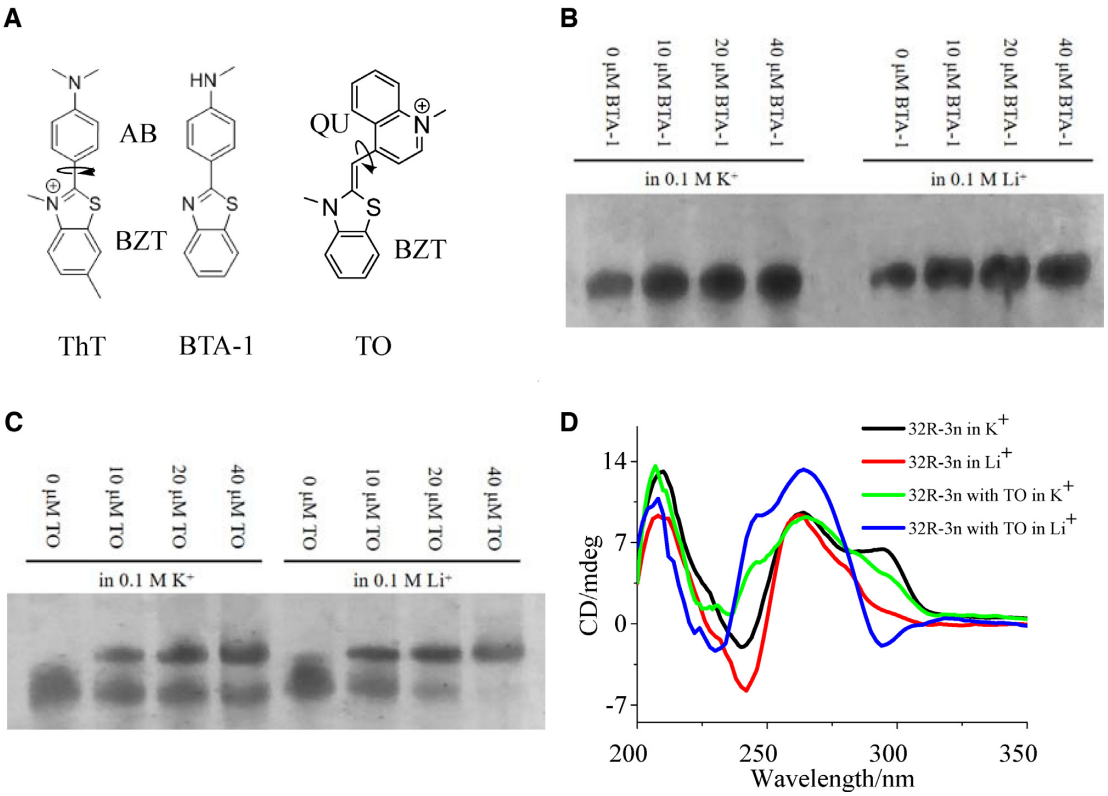

Figure 6. (**A**) Structures of ThT, TO and BTA-1. (**B** and **C**) Gel electrophoretograms of 32R-3n with or without (B) BTA-1 and (C) TO in 0.1 M K^+ or Li^+, respectively. (**D**) CD spectra of 32R-3n (8 μM) with or without 100 μM TO in 0.02 M Tris–HCl (pH 7.0) containing 0.1 M K^+ or Li^+.

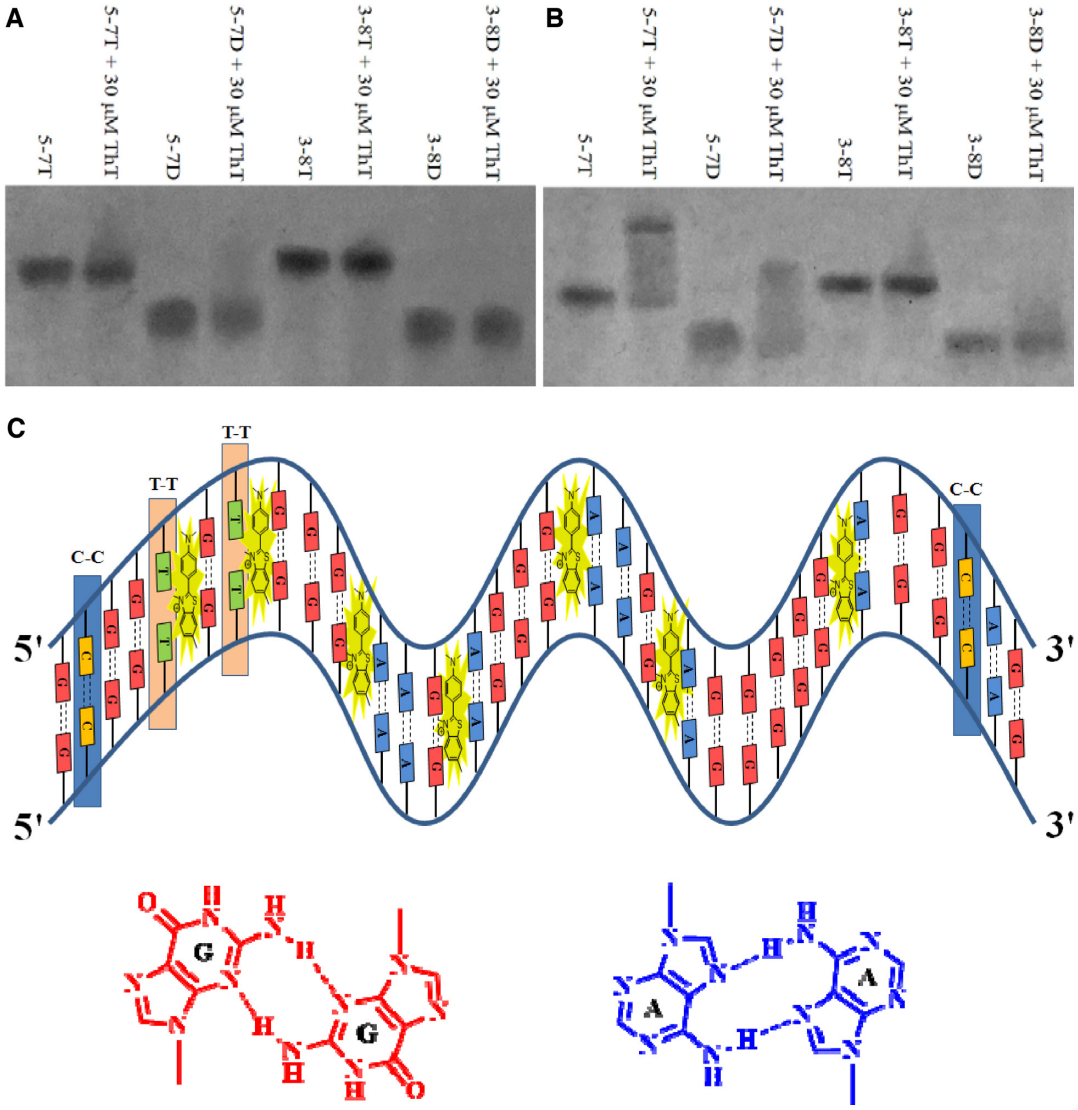

Figure 7. (**A** and **B**) Gel electrophoretograms of 5–7T, 5–7D, 3–8T and 3–8D (8 μM) in the absence and presence of 30 μM ThT in 0.1 M (A) K^+ and (B) Li^+, respectively. (**C**) Schematic diagram of the ThT clustering within psDNA. Also shown are the hydrogen-bonding patterns of G·G and A·A base pairs, as proposed in (2).

orescence by ∼75-fold (Supplementary Figure S9B). This binding in K^+ is able to form the 32R-3n dimer as demonstrated by the PAGE experiments (Figure 6C) in which increasing the TO concentration increased the slow-migration band and concurrently dimmed the G4 monomer band. This GF→psDNA switching seemed to be more explicit in Li^+ by the almost complete disappearance of the G4 monomer band with an increase in the TO concentration up to 40 μM. The CD experiments also revealed the structure switching in K^+ and Li^+ by TO binding (Figure 6D).

DISCUSSION

32R-3n forms the G4 structure in K^+ (Figure 1C) with the 7 nt overhang of 5′-GCGGTGT-3′ locating at the 5′ end (60). Therefore, we deleted this 5′ overhang from 32R-3n to obtain the remaining 25 nt 5–7D (Table 1). It seemed that 5–7D formed a similar G4 structure to 32R-3n in K^+, as demonstrated by the similar CD spectra (Supplementary Figure S10). However, ThT was inefficient in causing the dimer formation of 5–7D in K^+, while the Li^+ condition favored the dimer population with the presence of ThT (Figure 7A, B). Similarly, replacing the 7 nt overhang in 32R-3n with 5′-TTTTTTT-3′ (5–7T, Table 1) also supported the dimer formation, with a Li^+ over K^+ preference under the initiation of ThT (Figure 7A, B). These results suggest that this extra 7 nt overhang has a role to elicit the structure switching of the G4 folding of 32R-3n towards the dimer psDNA in K^+. This could be caused by the cooperative activity of the TG step of this overhang in forming the psDNA (Figure 7C), as demonstrated by Wang *et al.* (76). Recently, it has been reported that a truncated variant formed by removing 10 nt at the 3′ end of 32R and its mutant (22R and 22RT, Table 1) are also able to form G4 structures in K^+ (47–50). However, we found that although they also have the 7 nt 5′-GCGGTGT-3′, they cannot form

any dimer structure either in K^+ or in Li^+ with the presence of ThT (Supplementary Figure S11), suggesting the role of other sequences in determining the switching of G4 to psDNA. In addition, it has been reported that 32R-3n having base modifications can also have the potential to partially form the G4 structure with the 8 nt overhang of 5′-GGAGGCAG-3′ at the 3′ end (59). We thus deleted this 8 nt overhang from 32R-3n to obtain the 24 nt DNA of 3–8D (Table 1). Nevertheless, no dimer formation was observed for 3–8D in either K^+ or Li^+ solution (Figure 7A, B). The 8 nt 5′-TTTTTTTT-3′ replacement (3–8T, Table 1) also produced the same PAGE results as 3–8D, with no dimer formation (Figure 7A, B). These results indicate the role of sequence cooperativity in clustering ThT to form the psDNA structure.

The ITC method was then used to evaluate the clustering behaviors of ThT in switching G4 to psDNA. The typical ITC curves for 32R-3n in K^+ and Li^+ are presented in Supplementary Figure S12. Indeed, 32R-3n exhibited a quantitative binding with ThT in either K^+ or Li^+. The titration data presented a single sigmoidal contour (Supplementary Figure S12), suggesting that all of the strong binding sites in 32R-3n would not be greatly different with different ThT binding strength. Thus, we assumed roughly similar binding affinities of all sites for a given DNA, and the fitted thermodynamic results for all DNAs are listed in Table 2. Only the ThT binding with 32R-3n in K^+ was favored by both enthalpy and entropy, suggesting DNA structure switching. Furthermore, the DNAs having the potential to form dimer structures had roughly the same number of binding sites of 3.1–3.7 (32R-3n in K^+ and Li^+, and 32R, 5–7D, 5–7T in Li^+). Namely, most of these DNAs needed ∼6–7 ThT molecules to form the psDNA dimer structures, indicating the role of the multimolecular ThT clustering in generating the psDNA folding. Except for 32R-3n, other DNAs with the G4-forming potential in K^+ exhibited an almost 1:1 binding mode with ThT, implying intactness of G4 structures as confirmed with 32R, 22R and 22RT (47–50,60). Li *et al.* proposed that the 5′-GA-3′ steps in psDNA are the ThT-binding sites (2). Herein, we found that the investigated DNAs capable of forming the dimers in Li^+ always have five 5′-GA-3′ steps (32R-3n, 32R, 5–7T and 5–7D). However, those having only four 5′-GA-3′ steps (3–8T and 3–8D) lost the potential to be switched into the psDNA dimers by ThT. Furthermore, 22R and 22RT have only three and two 5′-GA-3′ steps, respectively. Nevertheless, the numbers of ThT-binding sites were 2.31 and 1.94 for these two DNAs in Li^+, as they were not able to form the dimer structures even in Li^+. These results imply that the 5′-GA-3′ steps are the ThT-binding sites and sufficient steps were needed to cluster ThT in registering the psDNA structures. The clustering binding of ThT with these five 5′-GA-3′ steps brings together the two strands of the dimer and subsequently supports the ThT binding in other post-available sites, as observed for 32R-3n that can otherwise bind seven ThT molecules in Li^+. It is likely that the 5′-most segment of 5′-GCGGTGTGG-3′ beyond the G4 core containing the five 5′-GA-3′ steps should have the potential to bind two ThT molecules (Figure 7C). For example, the 5′-TG-3′ step has been confirmed to play an important role in forming the psDNA dimer (76). However, although 32R has the same ThT binding steps of 5′-GA-3′ and 5′-TG-3′ as 32R-3n, the dimer structure of 32R can be formed only in Li^+, but not in K^+. Thus, it should be noted that this GF→psDNA switching can be performed only when the G4 stability is less than that of the psDNA upon ThT clustering, as demonstrated in Figure 2.

Table 2. The fitted thermodynamic parameters according to the ITC experiments

DNA	ion	*n* site	*K* 10^5/M	$\triangle H$ kcal/mol	$\triangle S$ cal/mol/deg	$\triangle G$ kcal/mol
32R-3n	K^+	3.10	0.71	–5.15	4.63	–6.50
	Li^+	3.68	1.02	–10.28	–12.1	–6.73
32R	K^+	0.89	0.35	–18.23	–41.4	–6.09
	Li^+	3.52	0.68	–13.65	–24.4	–6.50
3–8D	K^+	0.83	0.40	–12.02	–20.0	–6.16
	Li^+	2.78	0.30	–15.95	–33.9	–6.01
3–8T	K^+	0.84	0.42	–22.39	–55.2	–6.21
	Li^+	2.79	0.31	–20.12	–48.0	–6.05
5–7D	K^+	0.88	0.42	–14.74	–29.1	–6.21
	Li^+	3.35	0.58	–10.61	–14.4	–6.39
5–7T	K^+	0.85	0.39	–41.11	–119	–6.23
	Li^+	3.39	0.60	–14.25	–26.7	–6.42
22R	K^+	0.89	0.15	–19.61	–47.7	–5.63
	Li^+	2.31	0.45	–14.10	–26.8	–6.24
22RT	K^+	0.76	0.15	–42.85	–127	–5.61
	Li^+	1.94	0.44	–22.30	–54.8	–6.24

Since 32R-3n has two cytosines, the ThT-induced psDNA formation will provide the chance to form two C–C pairs (Figure 7C). In acidic solution, the C^+–C pairing should be expected when the psDNA is aligned by the ThT clustering. This will stabilize the psDNA structure further. The pH-dependent experiments shown in Figure 8A demonstrated that the presence of ThT increased the T_m values to a greater extent when acidifying the 32R-3n solution in K^+ in comparison with the ThT-free case, evidencing occurrence of the possible C^+–C pairing provided that the psDNA was formed. In addition, we found that the presence of Hg^{2+} also somewhat increased the T_m value of 32R-3n only when ThT was added (Figure 8B), since the formed psDNA had two T–T pairs for Hg^{2+} binding (Figure 7C). These results indicate that the psDNA formed by ThT clustering featured homo-base pairings (Figure 7C).

The above experiments indicate that 32R-3n adopting a hybrid G4 folding in K^+ can be switched into the psDNA structure by molecular rotors ThT and TO. However, we expect that this GF→psDNA switching can also be applied to G4s adopting other conformations. We again considered 32R with only a 3 nt frameshift in comparison with 32R-3n, as it adopts a parallel G4 conformation. Since the G4 stability of 32R is somewhat dependent on the K^+ concentration (54), we thus checked the effect of the K^+ concentration (0.005–0.1 M) on the G4 switching. Unfortunately, using ThT as the initiator cannot fulfill the GF→psDNA switching of 32R (Supplementary Figure S13) even at low K^+ concentration, since low-concentration salt will also destabilize the psDNA structure (85). However, it seemed that TO had a stronger binding with the psDNA structure of 32R than ThT, as confirmed by fluorescence titration carried out in Li^+ (Supplementary Figure S14), although the ITC experiments for predicting the precise binding site and the bind-

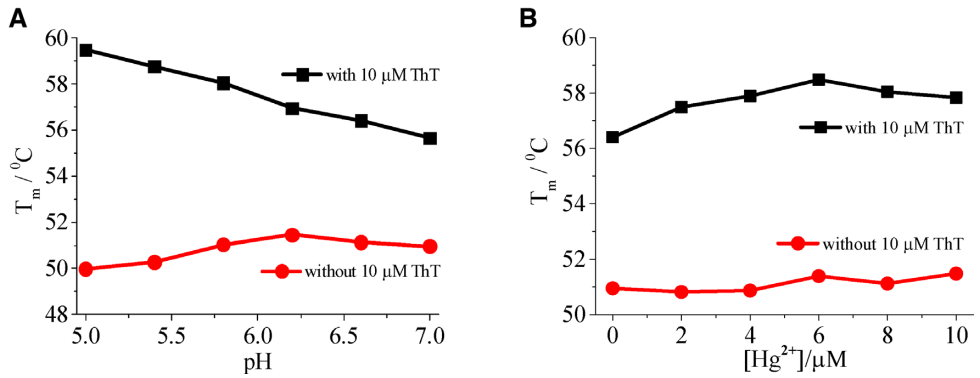

Figure 8. (**A**) T_m values of 32R-3n (4 μM) in 0.1 M K^+ as a function of pH in the absence and presence of ThT (10 μM), respectively. (**B**) T_m values of 32R-3n (4 μM) in 0.1 M K^+ as a function of the Hg^{2+} concentration in the absence and presence of ThT (10 μM) at pH 7.0. The T_m measurements were followed at 260 nm.

ing constant with TO were unsuccessful due to the obvious disturbance of the large heat of dilution caused by aggregation of TO in aqueous solution. We observed that TO was able to switch the parallel G4 folding of 32R into the psDNA structure (Supplementary Figure S13) within the investigated K^+ concentration range of 0.005–0.1 M. The slow-migration band in any K^+ concentration with the presence of TO had almost the same electrophoretic mobility as that obtained in Li^+, strongly suggesting psDNA formation. The TO clustering within the psDNA structure of 32R was confirmed in Li^+ by the Job's plot analysis (Supplementary Figure S14, ∼6–8 TO molecules/psDNA). This indicates that one can design molecular rotors having a strong binding competency with psDNA to realize the parallel G4 switching.

To explore other sequences that can be converted into homodimers from initially formed G4 structures by molecular rotors, we then investigated the nuclease-hypersensitive elements III_1 ($NHEIII_1$) from the c-*myc* gene (X12-1245 and X12-A3-2345, Table 1) that are also rich in the 5′-GA-3′ and 5′-TG-3′ steps. They adopt parallel G4 structures in K^+, and the abasic site (X) has been introduced to obtain the monomorphic G4 structures (97). We found that TO was much more efficient than ThT in inducing psDNAs of X12-1245 and X12-A3-2345 within the investigated K^+ concentration of 0.05–0.1 M, as observed by the PAGE experiments (Supplementary Figure S15). Similarly, TO had a stronger binding with the psDNA structures of these two DNAs than ThT as confirmed by fluorescence titration carried out in Li^+ (Supplementary Figure S16). Furthermore, it seemed that X12-A3-2345 in K^+ had a little more chance than X12-1245 of psDNA formation induced by ThT. This could be caused by the lower G4 stability of X12-A3-2345 than of X12-1245 (97). This G4 stability difference was also confirmed by the pyrene-labeled DNAs (X12-A3-2345-3P and X12-1245-3P, Table 1). X12-A3-2345-3P alone in K^+ led to a little more excimer emission in comparison with X12-1245-3P (although very small in quantity, Supplementary Figure S17). According to the method described in Figure 3, the excimer emission of the pyrene label was used to estimate the psDNA formation potency of these two G4s (Supplementary Figure S18). X12-1245-3P in K^+ led to a much weaker excimer emission relative to that obtained in Li^+ (e.g. ∼30% of the saturated excimer emission in Li^+ obtained at 8 μM ThT). However, X12-A3-2345-3P in K^+ showed a stronger excimer emission with respect to that obtained in Li^+ (e.g. ∼60% of the saturated excimer emission obtained in Li^+ even at 5 μM ThT). These are consistent with the PAGE results shown in Supplementary Figure S15. On the other hand, the ITC experiments evidenced the ThT clustering with the psDNA structures of X12-A3-2345 and X12-1245 formed in Li^+, respectively (Supplementary Figure S19, ∼5–6 ThT molecules/psDNA). The obtained binding thermodynamic parameters in Li^+ were comparable with the results corresponding to 32R-3n. Unfortunately, the overlapping of the excimer emission band of pyrene (∼480 nm) with the excitation band of TO (∼482 nm) impeded us from evaluating the psDNA formation using the excimer bands of X12-1245-3P and X12-A3-2345-3P. In this case, the TO emission band was used to examine the excimer to TO FRET under 348 nm excitation at which the bound TO was not directly excited (Supplementary Figure S9B). After subtracting the TO background emission in binding with the unlabeled DNAs (X12-1245 and X12-A3-2345), we indeed observed a decrease of the monomer bands of X12-1245-3P and X12-A3-2345-3P, and a concurrent increase of the TO bands upon binding of TO with these two labeled DNAs (Supplementary Figure S20), suggesting excimer to TO energy transfer. Subsequently, the TO clustering with X12-1245 and X12-A3-2345 was fluorescently confirmed in Li^+ by the Job's plot analysis (Supplementary Figure S21, ∼5–6 TO molecules/psDNA).

Lastly, it should be noted that although only DNA sequences were tested in this work, we expect that the G4 switching to a duplex would likewise occur for RNA sequences, if RNA G4s were less stable than the ligand-switched duplexes. Since stability of RNA G4s is usually higher than that of the corresponding DNA counterparts, this will need further efforts to screen ligands with high binding affinity for the parallel-stranded RNA duplexes. Nevertheless, we can imagine that short G4-forming RNA sequences (11), e.g. microRNAs, would be likewise converted by ligands having a strong clustering competency towards the RNA parallel duplexes. This will further

strengthen the biological significance of the G4 switching towards a parallel-stranded duplex.

DATA AVAILABILITY

All relevant data are included in the paper and/or its supplementary data.

SUPPLEMENTARY DATA

Supplementary Data are available at NAR Online.

FUNDING

This work was supported by the Key project of Natural Science Foundation of Zhejiang Province [LZ20B050001] the Leading Talent Program of Science and Technology Innovation in Zhejiang [2020R52022]; the National Natural Science Foundation of China [22274142, 21675142]; and the Independent Designing Scientific Research Project of Zhejiang Normal University [2020ZS0304]. Funding for open access charge: National Natural Science Foundation of China.
Conflict of interest statement. None declared.

REFERENCES

1. Szabat,M. and Kierzek,R. (2017) Parallel-stranded DNA and RNA duplexes—structural features and potential applications. *FEBS J.*, **284**, 3986–3998.
2. Liu,S., Peng,P., Wang,H., Shi,L. and Li,T. (2017) Thioflavin T binds dimeric parallel-stranded GA-containing non-G-quadruplex DNAs: a general approach to lighting up double-stranded scaffolds. *Nucleic Acids Res.*, **45**, 12080–12089.
3. Zhang,Y.P., Cui,Y.X., An,R., Liang,X.G., Li,Q., Wang,H.T., Wang,H., Fan,Y.Q., Dong,P., Li,J. *et al.* (2019) Topologically constrained formation of stable Z-DNA from normal sequence under physiological conditions. *J. Am. Chem. Soc.*, **141**, 7758–7764.
4. Kim,S.H., Lim,S.-H., Lee,A.-R., Kwon,D.H., Song,H.K., Lee,J.-H., Cho,M., Johner,A., Lee,N.-K. and Hong,S.-C. (2018) Unveiling the pathway to Z-DNA in the protein-induced B–Z transition. *Nucleic Acids Res.*, **46**, 4129–4137.
5. Zeraati,M., Langley,D.B., Schofield,P., Moye,A.L., Rouet,R., Hughes,W.E., Bryan,T.M., Dinger,M.E. and Christ,D. (2018) I-motif DNA structures are formed in the nuclei of human cells. *Nat. Chem.*, **10**, 631–637.
6. Abou Assi,H., Garavis,M., Gonzalez,C. and Damha,M.J. (2018) I-motif DNA: structural features and significance to cell biology. *Nucleic Acids Res.*, **46**, 8038–8056.
7. Tiwari,M.K., Adaku,N., Peart,N. and Rogers,F.A. (2016) Triplex structures induce DNA double strand breaks via replication fork collapse in NER deficient cells. *Nucleic Acids Res.*, **44**, 7742–7754.
8. Sakamoto,T., Yamaoki,Y., Nagata,T. and Katahira,M. (2021) Detection of parallel and antiparallel DNA triplex structures in living human cells using in-cell NMR. *Chem. Commun.*, **57**, 6364–6367.
9. Murat,P., Singh,Y. and Defrancq,E. (2011) Methods for investigating G-quadruplex DNA/ligand interactions. *Chem. Soc. Rev.*, **40**, 5293–5307.
10. Hansel-Hertsch,R., Beraldi,D., Lensing,S.V., Marsico,G., Zyner,K., Parry,A., Di Antonio,M., Pike,J., Kimura,H., Narita,M. *et al.* (2016) G-quadruplex structures mark human regulatory chromatin. *Nat. Genet.*, **48**, 1267–1272.
11. Tassinari,M., Richter,S.N. and Gandellini,P. (2021) Biological relevance and therapeutic potential of G-quadruplex structures in the human noncoding transcriptome. *Nucleic Acids Res.*, **49**, 3617–3633.
12. Bochman,M.L., Paeschke,K. and Zakian,V.A. (2012) DNA secondary structures: stability and function of G-quadruplex structures. *Nat. Rev. Genet.*, **13**, 770–780.
13. Varshney,D., Spiegel,J., Zyner,K., Tannahill,D. and Balasubramanian,S. (2020) The regulation and functions of DNA and RNA G-quadruplexes. *Nat. Rev. Mol. Cell Biol.*, **21**, 459–474.
14. Chen,J., Cheng,M., Salgado,G.F., Stadlbauer,P., Zhang,X., Amrane,S., Guedin,A., He,F., Sponer,J., Ju,H. *et al.* (2021) The beginning and the end: flanking nucleotides induce a parallel G-quadruplex topology. *Nucleic Acids Res.*, **49**, 9548–9559.
15. Cammas,A. and Millevoi,S. (2017) RNA G-quadruplexes: emerging mechanisms in disease. *Nucleic Acids Res.*, **45**, 1584–1595.
16. Neidle,S. (2016) Quadruplex nucleic acids as novel therapeutic targets. *J. Med. Chem.*, **59**, 5987–6011.
17. Marchand,A. and Gabelica,V. (2016) Folding and misfolding pathways of G-quadruplex DNA. *Nucleic Acids Res.*, **44**, 10999–11012.
18. Bao,H.-L., Liu,H.-S. and Xu,Y. (2019) Hybrid-type and two-tetrad antiparallel telomere DNA G-quadruplex structures in living human cells. *Nucleic Acids Res.*, **47**, 4940–4947.
19. Maldonado,R., Schwartz,U., Silberhorn,E. and Laengst,G. (2019) Nucleosomes stabilize ssRNA–dsDNA triple helices in human cells. *Mol. Cell*, **73**, 1243–1254.
20. Shi,L., Peng,P., Du,Y. and Li,T. (2017) Programmable i-motif DNA folding topology for a pH-switched reversible molecular sensing device. *Nucleic Acids Res.*, **45**, 4306–4314.
21. Hahn,J. and Shih,W.M. (2019) Thermal cycling of DNA devices via associative strand displacement. *Nucleic Acids Res.*, **47**, 10968–10975.
22. Sutherland,C., Cui,Y., Mao,H. and Hurley,L.H. (2016) A mechanosensor mechanism controls the G-quadruplex/i-motif molecular switch in the MYC promoter NHE III_1. *J. Am. Chem. Soc.*, **138**, 14138–14151.
23. Abou Assi,H., Harkness,R.W., Martin-Pintado,N., Wilds,C.J., Campos-Olivas,R., Mittermaier,A.K., Gonzalez,C. and Damha,M.J. (2016) Stabilization of i-motif structures by 2'-beta-fluorination of DNA. *Nucleic Acids Res.*, **44**, 4998–5009.
24. Fan,D., Wang,J., Wang,E. and Dong,S. (2020) Propelling DNA computing with materials' power: recent advancements in innovative DNA logic computing systems and smart bio-applications. *Adv. Sci.*, **7**, 2001766.
25. Li,Q., Fei,Y., Gao,L., Yu,Y., Zhou,Y., Ye,T., Zhou,X.-S., Shao,Y. and Yin,Z.-Z. (2018) G-quadruplex DNA with an apurinic site as a soft molecularly imprinted sensing platform. *Anal. Chem.*, **90**, 5552–5556.
26. Babinsky,M., Fiala,R., Kejnovska,I., Bednarova,K., Marek,R., Sagi,J., Sklenar,V. and Vorlickova,M. (2014) Loss of loop adenines alters human telomere $d[AG_3(ttag_3)_3]$ quadruplex folding. *Nucleic Acids Res.*, **42**, 14031–14041.
27. Takahashi,S., Kim,K.T., Podbevsek,P., Plavec,J., Kim,B.H. and Sugimoto,N. (2018) Recovery of the formation and function of oxidized G-quadruplexes by a pyrene-modified guanine tract. *J. Am. Chem. Soc.*, **140**, 5774–5783.
28. Filitcheva,J., Edwards,P.J.B., Norris,G.E. and Filichev,V.V. (2019) α-2'-Deoxyguanosine can switch DNA G-quadruplex topologies from antiparallel to parallel. *Org. Biomol. Chem.*, **17**, 4031–4042.
29. Idili,A., Vallée-Bélisle,A. and Ricci,F. (2014) Programmable pH-triggered DNA nanoswitches. *J. Am. Chem. Soc.*, **136**, 5836–5839.
30. Galer,P., Wang,B., Sket,P. and Plavec,J. (2016) Reversible pH switch of two-quartet G-quadruplexes formed by human telomere. *Angew. Chem. Int. Ed.*, **55**, 1993–1997.
31. Mamajanov,I., Engelhart,A.E., Bean,H.D. and Hud,N.V. (2010) DNA and RNA in anhydrous media: duplex, triplex, and G-quadruplex secondary structures in a deep eutectic solvent. *Angew. Chem. Int. Ed.*, **49**, 6310–6314.
32. Zhao,C., Ren,J. and Qu,X. (2013) G-quadruplexes form ultrastable parallel structures in deep eutectic solvent. *Langmuir*, **29**, 1183–1191.
33. Lannan,F.M., Mamajanov,I. and Hud,N.V. (2012) Human telomere sequence DNA in water-free and high-viscosity solvents: G-quadruplex folding governed by Kramers rate theory. *J. Am. Chem. Soc.*, **134**, 15324–15330.
34. Xue,Y., Kan,Z.-y., Wang,Q., Yao,Y., Liu,J., Hao,Y.-h. and Tan,Z. (2007) Human telomeric DNA forms parallel-stranded intramolecular G-quadruplex in K^+ solution under molecular crowding condition. *J. Am. Chem. Soc.*, **129**, 11185–11191.
35. Heddi,B. and Phan,A.T. (2011) Structure of human telomeric DNA in crowded solution. *J. Am. Chem. Soc.*, **133**, 9824–9833.

36. Miyoshi,D., Nakao,A. and Sugimoto,N. (2002) Molecular crowding regulates the structural switch of the DNA G-quadruplex. *Biochemistry*, **41**, 15017–15024.
37. Kim,Y., Phillips,J.A., Liu,H., Kang,H. and Tan,W. (2009) Using photons to manipulate enzyme inhibition by an azobenzene-modified nucleic acid probe. *Proc. Natl Acad. Sci. USA.*, **106**, 6489–6494.
38. Ogasawara,S. and Maeda,M. (2009) Reversible photoswitching of a G-quadruplex. *Angew. Chem. Int. Ed.*, **48**, 6671–6674.
39. Mendoza,O., Bourdoncle,A., Boule,J.-B., Brosh,R.M. Jr and Mergny,J.-L. (2016) G-quadruplexes and helicases. *Nucleic Acids Res.*, **44**, 1989–2006.
40. Lejault,P., Mitteaux,J., Sperti,F.R. and Monchaud,D. (2021) How to untie G-quadruplex knots and why?*Cell Chem. Biol.*, **28**, 436–455.
41. Mitteaux,J., Lejault,P., Wojciechowski,F., Joubert,A., Boudon,J., Desbois,N., Gros,C.P., Hudson,R.H.E., Boule,J.-B., Granzhan,A. *et al.* (2021) Identifying G-quadruplex-DNA-disrupting small molecules. *J. Am. Chem. Soc.*, **143**, 12567–12577.
42. Waller,Z.A.E., Sewitz,S.A., Hsu,S.-T.D. and Balasubramanian,S. (2009) A small molecule that disrupts G-quadruplex DNA structure and enhances gene expression. *J. Am. Chem. Soc.*, **131**, 12628–12633.
43. Wang,X., Huang,J., Zhou,Y., Yan,S., Weng,X., Wu,X., Deng,M. and Zhou,X. (2010) Conformational switching of G-quadruplex DNA by photoregulation. *Angew. Chem. Int. Ed.*, **49**, 5305–5309.
44. Tian,T., Song,Y., Wei,L., Wang,J., Fu,B., He,Z., Yang,X.-R., Wu,F., Xu,G., Liu,S.-M. *et al.* (2017) Reversible manipulation of the G-quadruplex structures and enzymatic reactions through supramolecular host–guest interactions. *Nucleic Acids Res.*, **45**, 2283–2293.
45. O'Hagan,M.P., Haldar,S., Duchi,M., Oliver,T.A.A., Mulholland,A.J., Morales,J.C. and Galan,M.C. (2019) A photoresponsive stiff-stilbene ligand fuels the reversible unfolding of G-quadruplex DNA. *Angew. Chem. Int. Ed.*, **58**, 4334–4338.
46. Zhou,Y., Yu,Y., Gao,L., Fei,Y., Ye,T., Li,Q., Zhou,X., Gan,N. and Shao,Y. (2018) Structuring polarity-inverted TBA to G-quadruplex for selective recognition of planarity of natural isoquinoline alkaloids. *Analyst*, **143**, 4907–4914.
47. Kerkour,A., Marquevielle,J., Ivashchenko,S., Yatsunyk,L.A., Mergny,J.-L. and Salgado,G.F. (2017) High-resolution three-dimensional NMR structure of the KRAS proto-oncogene promoter reveals key features of a G-quadruplex involved in transcriptional regulation. *J. Biol. Chem.*, **292**, 8082–8091.
48. Ou,A., Schmidberger,J.W., Wilson,K.A., Evans,C.W., Hargreaves,J.A., Grigg,M., O'Mara,M.L., Iyer,K.S., Bond,C.S. and Smith,N.M. (2020) High resolution crystal structure of a KRAS promoter G-quadruplex reveals a dimer with extensive poly-A π-stacking interactions for small-molecule recognition. *Nucleic Acids Res.*, **48**, 5766–5776.
49. D'Aria,F., Pagano,B., Petraccone,L. and Giancola,C. (2021) KRAS promoter G-quadruplexes from sequences of different length: a physicochemical study. *Int. J. Mol. Sci.*, **22**, 448.
50. Carvalho,J., Pereira,E., Marquevielle,J., Campello,M.P.C., Mergny,J.-L., Paulo,A., Salgado,G.F., Queiroz,J.A. and Cruz,C. (2018) Fluorescent light-up acridine orange derivatives bind and stabilize KRAS-22RT G-quadruplex. *Biochimie*, **144**, 144–152.
51. Morgan,R.K., Batra,H., Gaerig,V.C., Hockings,J. and Brooks,T.A. (2016) Identification and characterization of a new G-quadruplex forming region within the kRAS promoter as a transcriptional regulator. *Biochim. Biophys. Acta*, **1859**, 235–245.
52. Paramasivam,M., Membrino,A., Cogoi,S., Fukuda,H., Nakagama,H. and Xodo,L.E. (2009) Protein hnRNP A1 and its derivative Up1 unfold quadruplex DNA in the human KRAS promoter: implications for transcription. *Nucleic Acids Res.*, **37**, 2841–2853.
53. Cogoi,S., Rapozzi,V., Cauci,S. and Xodo,L.E. (2017) Critical role of hnRNP A1 in activating KRAS transcription in pancreatic cancer cells: a molecular mechanism involving G4 DNA. *Biochim. Biophys. Acta*, **1861**, 1389–1398.
54. Cogoi,S., Paramasivam,M., Spolaore,B. and Xodo,L.E. (2008) Structural polymorphism within a regulatory element of the human KRAS promoter: formation of G4-DNA recognized by nuclear proteins. *Nucleic Acids Res.*, **36**, 3765–3780.
55. Cogoi,S. and Xodo,L.E. (2006) G-quadruplex formation within the promoter of the KRAS proto-oncogene and its effect on transcription. *Nucleic Acids Res.*, **34**, 2536–2549.
56. Kaiser,C.E., Van Ert,N.A., Agrawal,P., Chawla,R., Yang,D. and Hurley,L.H. (2017) Insight into the complexity of the i-motif and G-quadruplex DNA structures formed in the KRAS promoter and subsequent drug induced gene repression. *J. Am. Chem. Soc.*, **139**, 8522–8536.
57. Cogoi,S., Ferino,A., Miglietta,G., Pedersen,E.B. and Xodo,L.E. (2018) The regulatory G4 motif of the kirsten ras (KRAS) gene is sensitive to guanine oxidation: implications on transcription. *Nucleic Acids Res.*, **46**, 661–676.
58. Marquevielle,J., Robert,C., Lagrabette,O., Wahid,M., Bourdoncle,A., Xodo,L.E., Mergny,J.-L. and Salgado,G.F. (2020) Structure of two G-quadruplexes in equilibrium in the KRAS promoter. *Nucleic Acids Res.*, **48**, 9336–9345.
59. Cogoi,S., Zorzet,S., Rapozzi,V., Geci,I., Pedersen,E.B. and Xodo,L.E. (2013) MAZ-binding G4-decoy with locked nucleic acid and twisted intercalating nucleic acid modifications suppresses KRAS in pancreatic cancer cells and delays tumor growth in mice. *Nucleic Acids Res.*, **41**, 4049–4064.
60. Cogoi,S., Paramasivam,M., Filichev,V., Geci,I., Pedersen,E.B. and Xodo,L.E. (2009) Identification of a new G-quadruplex motif in the KRAS promoter and design of pyrene-modified G4-decoys with antiproliferative activity in pancreatic cancer cells. *J. Med. Chem.*, **52**, 564–568.
61. Podbevsek,P. and Plavec,J. (2016) KRAS promoter oligonucleotide with decoy activity dimerizes into a unique topology consisting of two G-quadruplex units. *Nucleic Acids Res.*, **44**, 917–925.
62. Rigo,R., Palumbo,M. and Sissi,C. (2017) G-quadruplexes in human promoters: a challenge for therapeutic applications. *Biochim. Biophys. Acta*, **1861**, 1399–1413.
63. Wu,H.-Z., Xiao,J.-Q., Xiao,S.-S. and Cheng,Y. (2019) KRAS: a promising therapeutic target for cancer treatment. *Curr. Top. Med. Chem.*, **19**, 2081–2097.
64. Verma,S., Ravichandiran,V. and Ranjan,N. (2021) Beyond amyloid proteins: thioflavin T in nucleic acid recognition. *Biochimie*, **190**, 111–123.
65. Liu,L., Shao,Y., Peng,J., Liu,H. and Zhang,L. (2013) Selective recognition of ds-DNA cavities by a molecular rotor: switched fluorescence of thioflavin T. *Mol. Biosyst.*, **9**, 2512–2519.
66. Shi,L., Peng,P., Zheng,J., Wang,Q., Tian,Z., Wang,H. and Li,T. (2020) I-motif/miniduplex hybrid structures bind benzothiazole dyes with unprecedented efficiencies: a generic light-up system for label-free DNA nanoassemblies and bioimaging. *Nucleic Acids Res.*, **48**, 1681–1690.
67. Zhou,W., Yu,Z., Ma,G., Jin,T., Li,Y., Fan,L. and Li,X. (2019) Thioflavin T specifically brightening 'guanine island' in duplex-DNA: a novel fluorescent probe for single-nucleotide mutation. *Analyst*, **144**, 2284–2290.
68. Pramanik,S., Nandy,A., Chakraborty,S., Pramanik,U., Nandi,S. and Mukherjee,S. (2020) Preferential binding of thioflavin T to AT-rich DNA: white light emission through intramolecular Forster resonance energy transfer. *J. Phys. Chem. Lett.*, **11**, 2436–2442.
69. Wang,H., Wang,J., Xu,L., Zhang,Y., Chen,Y., Chen,H. and Pei,R. (2016) Selection and characterization of thioflavin T aptamers for the development of light-up probes. *Anal. Methods*, **8**, 8461–8465.
70. Lee,I.J., Patil,S.P., Fhayli,K., Alsaiari,S. and Khashab,N.M. (2015) Probing structural changes of self assembled i-motif DNA. *Chem. Comm.*, **51**, 3747–3749.
71. Liu,L., Shao,Y., Peng,J., Huang,C., Liu,H. and Zhang,L. (2014) Molecular rotor-based fluorescent probe for selective recognition of hybrid G-quadruplex and as a K^+ sensor. *Anal. Chem.*, **86**, 1622–1631.
72. Mohanty,J., Barooah,N., Dhamodharan,V., Harikrishna,S., Pradeepkumar,P.I. and Bhasikuttan,A.C. (2013) Thioflavin T as an efficient inducer and selective fluorescent sensor for the human telomeric G-quadruplex DNA. *J. Am. Chem. Soc.*, **135**, 367–376.
73. Jing,S., Liu,Q., Jin,Y. and Li,B. (2021) Dimeric G-quadruplex: an effective nucleic acid scaffold for lighting up thioflavin T. *Anal. Chem.*, **93**, 1333–1341.
74. Lubitz,I., Zikich,D. and Kotlyar,A. (2010) Specific high-affinity binding of thiazole orange to triplex and G-quadruplex DNA. *Biochemistry*, **49**, 3567–3574.
75. Monchaud,D., Allain,C. and Teulade-Fichou,M.P. (2007) Thiazole orange: a useful probe for fluorescence sensing of

G-quadruplex–ligand interactions. *Nucleosides Nucleotides Nucleic Acids*, **26**, 1585–1588.
76. Zhu,J., Yan,Z., Zhou,W., Liu,C., Wang,J. and Wang,E. (2018) Lighting up the thioflavin T by parallel-stranded TG(GA)$_n$ DNA homoduplexes. *ACS Sens.*, **3**, 1118–1125.
77. Liu,Q., Jing,S., Liu,M., Jin,Y. and Li,B. (2020) Parallel [TG(GA)$_3$]$_n$-homoduplexes/thioflavin T: an intense and stable fluorescent indicator for label-free biosensing. *Analyst*, **145**, 286–294.
78. Hanczyc,P., Rajchel-Mieldzioc,P., Feng,B. and Fita,P. (2021) Identification of thioflavin T binding modes to DNA: a structure-specific molecular probe for lasing applications. *J. Phys. Chem. Lett.*, **12**, 5436–5442.
79. Mergny,J.L., Phan,A.T. and Lacroix,L. (1998) Following G-quartet formation by UV-spectroscopy. *FEBS Lett.*, **435**, 74–78.
80. Paiva,A.M. and Sheardy,R.D. (2005) The influence of sequence context and length on the kinetics of DNA duplex formation from complementary hairpins possessing (CNG) repeats. *J. Am. Chem. Soc.*, **127**, 5581–5585.
81. Fodera,V., Groenning,M., Vetri,V., Librizzi,F., Spagnolo,S., Cornett,C., Olsen,L., van de Weert,M. and Leone,M. (2008) Thioflavin T hydroxylation at basic pH and its effect on amyloid fibril detection. *J. Phys. Chem. B*, **112**, 15174–15181.
82. Xing,F., Song,G., Ren,J., Chaires,J.B. and Qu,X. (2005) Molecular recognition of nucleic acids: coralyne binds strongly to poly(A). *FEBS Lett.*, **579**, 5035–5039.
83. Karsisiotis,A.I., Hessari,N.M., Novellino,E., Spada,G.P., Randazzo,A. and Webba da Silva,M. (2011) Topological characterization of nucleic acid G-quadruplexes by UV absorption and circular dichroism. *Angew. Chem. Int. Ed.*, **50**, 10645–10648.
84. Kypr,J., Kejnovska,I., Renciuk,D. and Vorlickova,M. (2009) Circular dichroism and conformational polymorphism of DNA. *Nucleic Acids Res.*, **37**, 1713–1725.
85. Rippe,K., Fritsch,V., Westhof,E. and Jovin,T.M. (1992) Alternating d(G-A) sequences form a parallel-stranded DNA homoduplex. *EMBO J.*, **11**, 3777–3786.
86. Robinson,H., van Boom,J.H. and Wang,A.H.J. (1994) 5′-CGA motif induces other sequences to form homo base-paired parallel-stranded DNA duplex: the structure of (G-A)$_n$ derived from four DNA oligomers containing (G-A)$_3$ sequence. *J. Am. Chem. Soc.*, **116**, 1565–1566.
87. Dolinnaya,N.G., Ulku,A. and Fresco,J.R. (1997) Parallel-stranded linear homoduplexes of d(A^+-A)$_{n>10}$ and d(A-G)$_{n>10}$ manifesting the contrasting ionic strength sensitivities of poly(A^+·A^+) and DNA. *Nucleic Acids Res.*, **25**, 1100–1107.
88. Garbett,N.C., Ragazzon,P.A. and Chaires,J.B. (2007) Circular dichroism to determine binding mode and affinity of ligand–DNA interactions. *Nat. Protoc.*, **2**, 3166–3172.
89. Zhu,H. and Lewis,F.D. (2007) Pyrene excimer fluorescence as a probe for parallel G-quadruplex formation. *Bioconjugate Chem.*, **18**, 1213–1217.
90. Sulatskaya,A.I., Kuznetsova,I.M. and Turoverov,K.K. (2012) Interaction of thioflavin T with amyloid fibrils: fluorescence quantum yield of bound dye. *J. Phys. Chem. B*, **116**, 2538–2544.
91. Singh,P.K., Kumbhakar,M., Pal,H. and Nath,S. (2010) Viscosity effect on the ultrafast bond twisting dynamics in an amyloid fibril sensor: thioflavin-T. *J. Phys. Chem. B*, **114**, 5920–5927.
92. Stsiapura,V.I., Maskevich,A.A., Tikhomirov,S.A. and Buganov,O.V. (2010) Charge transfer process determines ultrafast excited state deactivation of thioflavin T in low-viscosity solvents. *J. Phys. Chem. A*, **114**, 8345–8350.
93. Maskevich,A.A., Stsiapura,V.I., Kuzmitsky,V.A., Kuznetsova,I.M., Povarova,O.I., Uversky,V.N. and Turoverov,K.K. (2007) Spectral properties of thioflavin T in solvents with different dielectric properties and in a fibril-incorporated form. *J. Proteome Res.*, **6**, 1392–1401.
94. Lai,H.-P., Gao,R.-C., Huang,C.-L., Chen,I.C. and Tan,K.-T. (2015) Fluorescence switchable probes based on a molecular rotor for selective detection of proteins and small molecules. *Chem. Comm.*, **51**, 16197–16200.
95. Gautam,R.K., Bapli,A., Jana,R. and Seth,D. (2021) Photophysics of thiazole orange in deep eutectic solvents. *Spectrochim. Acta A*, **258**, 119812.
96. Cao,J., Wu,T., Hu,C., Liu,T., Sun,W., Fan,J. and Peng,X. (2012) The nature of the different environmental sensitivity of symmetrical and unsymmetrical cyanine dyes: an experimental and theoretical study. *Phys. Chem. Chem. Phys.*, **14**, 13702–13708.
97. Beckett,J., Burns,J., Broxson,C. and Tornaletti,S. (2012) Spontaneous DNA lesions modulate DNA structural transitions occurring at nuclease hypersensitive element III$_1$ of the human c-myc proto-oncogene. *Biochemistry*, **51**, 5257–5268.